and stable oxide, is also bio-inert. Its wide bandgap energy (from 4 to 6 eV depending on polymorph nature[29]) associated with a relative low phonon cut-off energy constitute relevant physical properties to consider zirconia as a promising material for the production of efficient lanthanides doped phosphors.[30–32] The applications of this or other oxide hosts in bio-applications, including as bio-imaging agents, require the production of high quality doped nanoparticles which can be further functionalized into biological labels. This way, the search for new approaches to synthesize improved doped nanoparticles in an easy and low cost way is increasing. Several chemical and physical methods have been used to produce UC nanophosphors.[3,7,33] Recently, pulsed laser ablation in liquids (PLAL) arises as a reliable technique to produce nanomaterials.[34–38] In this technique a high power pulsed laser is used to irradiated a solid target, immersed in an appropriated liquid medium. PLAL allows the formation of chemical pure and stable nanoparticles in a liquid medium. Moreover, the simplicity and the low cost of the process associated with the absence of chemical reagents or ligands increases the interest of this method to produce metal, oxides, or even core–shell nanoparticles. The control of laser parameters and the nature of surrounding media allows manipulate the size, shape, chemical composition and functional properties of the nanoparticles (NPs). The synthesis of Ln^{3+} doped oxides nanoparticles, such as YAG and Y_2O_3 by PLAL were already reported in literature.[39–45] However, it is noteworthy that although there are studies on zirconia nanoparticles produced by PLAL, all works are about undoped zirconia.[46–49] Thus, the work here presented regarding erbium doped zirconia nanoparticles produced by pulsed laser ablation in water, constitutes a novelty, as far as we know. The spectroscopic characteristics of prompt and up conversion luminescence of the ZrO_2:Er^{3+} nanoparticles and targets are analyzed in detail by means of energy and excitation dependent steady state photoluminescence (PL) and photoluminescence excitation (PLE). With a $4f^{11}$ electron configuration Er^{3+} ions introduce a wide range of energetic levels in the zirconia band gap allowing the observation of the parity forbidden intra-4f transitions from the visible to infrared. Besides the well-known infrared ~1.54 μm $^4I_{13/2} \rightarrow {}^4I_{15/2}$ emission, visible light in the green and red spectral regions can be achieved *via* the $^4S_{3/2} \rightarrow {}^4I_{15/2}$ and $^4F_{9/2} \rightarrow {}^4I_{15/2}$ multiplet transitions, respectively, namely under infrared photon excitation, which is of interest for the aforementioned luminescent-based biosensors.

2. Experimental

Laser ablation was performed using a nanosecond Q-switched Nd:YAG laser with 1064 nm wavelength photons, 10 Hz pulse repetition rate and 7 ns pulse width. The maximum pulse energy is 685 mJ on a focus area of 0.38 cm^2. The ceramic ZrO_2:Er targets were placed in the bottom of a cell immersed in distilled water as shown in Fig. 1.

The height of water column above the target was kept constant at ~10 mm. The ceramic targets were prepared through the uniaxial pressing and densification of Er^{3+} doped

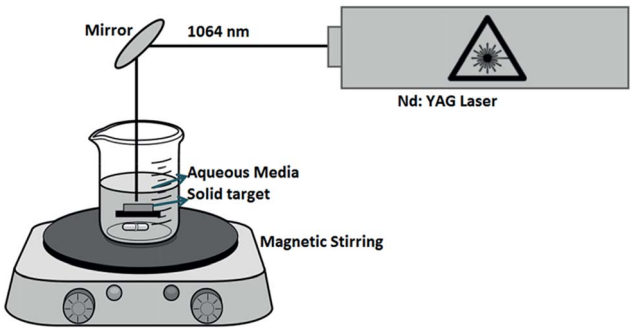

Fig. 1 Experimental setup used in PLAL technique.

ZrO_2 powders prepared by solution combustion synthesis (CS). In CS process, a solution of metal nitrates and an organic fuel (urea) was heated at 450 °C to promote auto-ignition of the solution and the production of the powders as described elsewhere.[50] For the ZrO_2:Er^{3+} samples the nominal Er^{3+} concentration was changed from 1 to 16 mol%. The produced powders were uniaxial pressed into pellets and heat treated at 1350 °C for 3 days to promote densification. The ceramic targets were taken as reference samples for the measured optical properties. The samples characteristics analyzed in this work are summarized in Table 1.

For the crystalline phase identification, the targets and NPs were analyzed by RT Raman spectroscopy performed under backscattering geometry with the 325 nm line of a He–Cd laser as excitation, using a Jobin-Yvon HR800 system. The samples morphology was analyzed by scanning electron microscopy/scanning transmission electron microscopy (SEM/STEM) on Hitachi SU-70 equipment. Energy Dispersive X-ray Spectroscopy (EDS) analysis were performed in the SEM, for chemical elemental identification. The samples luminescence was assessed at RT using ultraviolet, visible and infrared light as excitation, enabling the analysis of prompt and up converted intraionic emission. Moreover, the identification of the preferential ion luminescence excitation pathways was measured by RT PLE. Dispersive systems were used in the PL and PLE measurements fitted with cooled Hamamatsu R928 photomultiplier tubes. In the first case a SPEX 1704 monochromator (1 m, 1200 g mm^{-1}) was used whereas the PLE spectra were recorded in a Fluorolog-3 Horiba Scientific modular equipment with a double additive grating scanning monochromator (2 × 180 mm, 1200 g mm^{-1}) in the excitation and a triple grating iHR550 spectrograph in the emission (550 mm, 1200 g mm^{-1}). The measurements were realized using a front face acquisition mode, and were corrected to the optical components and to the Xe lamp spectral responses.

3. Results and discussion

3.1. Structural, morphological and compositional analysis

Fig. 2 shows the Raman spectra of the ceramic targets and the PLAL produced ZrO_2 nanoparticles doped with different nominal erbium amounts. As expected, the number of Raman active modes decreases with the rise of dopant content due to

Table 1 Summary of synthesis conditions of the studied samples

Sample name	Nominal dopant concentration	Preparation	Detected phases
Target ZrO_2:1Er	1 mol% Er	Targets produced by sintering of CS powders	Monoclinic
Target ZrO_2:2Er	2 mol% Er		Monoclinic
Target ZrO_2:5Er	5 mol% Er		Monoclinic and tetragonal
Target ZrO_2:10Er	10 mol% Er		Tetragonal
Target ZrO_2:16Er	16 mol% Er		Cubic
NPs ZrO_2:1Er	1 mol% Er	NPs produced by pulsed laser ablation in liquid	Monoclinic and tetragonal
NPs ZrO_2:2Er	2 mol% Er		Monoclinic and tetragonal
NPs ZrO_2:5Er	5 mol% Er		Monoclinic and tetragonal
NPs ZrO_2:10Er	10 mol% Er		Tetragonal
NPs ZrO_2:16Er	16 mol% Er		Cubic

increase of the zirconia crystal symmetry with the phase transformation from monoclinic to tetragonal and to cubic.[51] For the monoclinic phase (C_{2h}), the one stable at RT and ambient pressure for pure zirconia, 18 Raman active vibrational modes are predicted by group theory ($9A_g + 9B_g$) in the Γ point of the first Brillouin zone.[51] For the high temperature tetragonal and cubic zirconia phases, stabilized with increasing dopant amount, group theory predicts 6 fundamental Raman active modes ($1A_{1g} + 2B_{1g} + 3E_g$) for the tetragonal phase (D_{4h}), whereas in the case of cubic zirconia (O_h) only one Raman active vibrational mode (F_{2g}) is expected.[51]

As evidenced in the Raman spectra shown in Fig. 2 – left, ceramic target doped with the lower Er^{3+} concentration (1 mol%) crystallizes in the monoclinic phase of zirconia. Increasing erbium concentration favors the stabilization of the high temperature phases at RT. A mixture of monoclinic and tetragonal phases were found for the intermediate contents (2–5 mol% of Er^{3+}), and for nominal concentrations of 10 and 16 mol% Er^{3+} the Raman spectra evidence that zirconia doped targets crystallizes in tetragonal and cubic phases, respectively. These results, regarding the crystalline phase identification were corroborated by powders X-ray diffraction analysis (not shown). The main phases identified in the nanoparticles perfectly match those of the reference targets for the high dopant concentrations, where only the high temperature phases are present. In the case of lower dopant concentrations, additionally to the monoclinic phase identified in the targets, nanoparticles crystallized in the tetragonal phase were also present. This mismatch in the crystalline phases in the targets and NPs can be explained based in the existence of additional pathways to stabilize the high temperature metastable zirconia phases in the NPs. As well reported in literature, these phases can be stabilized in pure zirconia by reducing the particle size below a critical value.[52–54] No secondary crystalline phases, such as Er_2O_3 or other Er based oxide, were detected, even for the nominal high dopant concentrations, meaning that the PLAL process allows an efficient incorporation of the ion in the zirconia lattice.

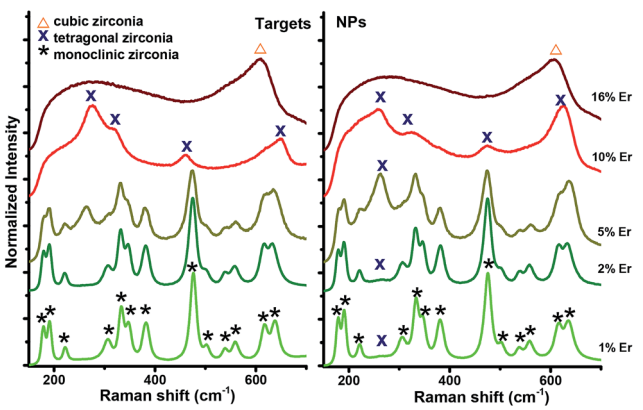

Fig. 2 Raman spectra of the targets (left) and PLAL produced NPs (right) by using 325 nm wavelength excitation in backscattering geometry.

The morphology and grain size of the doped zirconia nanoparticles is shown in Fig. 3. The STEM images reveal that the PLAL produced ZrO_2 nanoparticles have spherical shape with reduced dimensions as expected for a very fast process far from-equilibrium due to the narrow quenching times. These results agree well with the previous reported data by H. Zeng *et al.*[37] where the particle dimensions were directly related with the plasma plume cooling rate. In fact, the size of the synthesized nanocrystals is at the nanometer scale, when the quenching time of the plasma plume is of the order of nanoseconds. However, as can be observed in the STEM images, the formed NPs have a large size distribution and a high degree of agglomeration, particularly in the smaller ones. This behavior is a typical characteristic in NPs produced by PLAL.[55,56] This problem can be, apparently, overpassed through the control and optimization of growth parameters. In fact, in the last years worldwide researchers focus their attention on the size control of both metal, and oxide nanoparticles, produced by the PLAL as reported in the literature.[57,58] Parameters such as laser wavelength, laser fluence, time of irradiation, height of liquid above the target, addition of surfactants, pH of the liquid medium and angle between target and laser beam, seems to influence, at different scales, both the average particle size and size distribution of produced NPs. Some examples are the works reported by the S. A. Al-Mamun *et al.*[58,59] in which they studied almost all these parameters for the case Al_2O_3 NPs produced by PLAL in water, yielding to narrower size

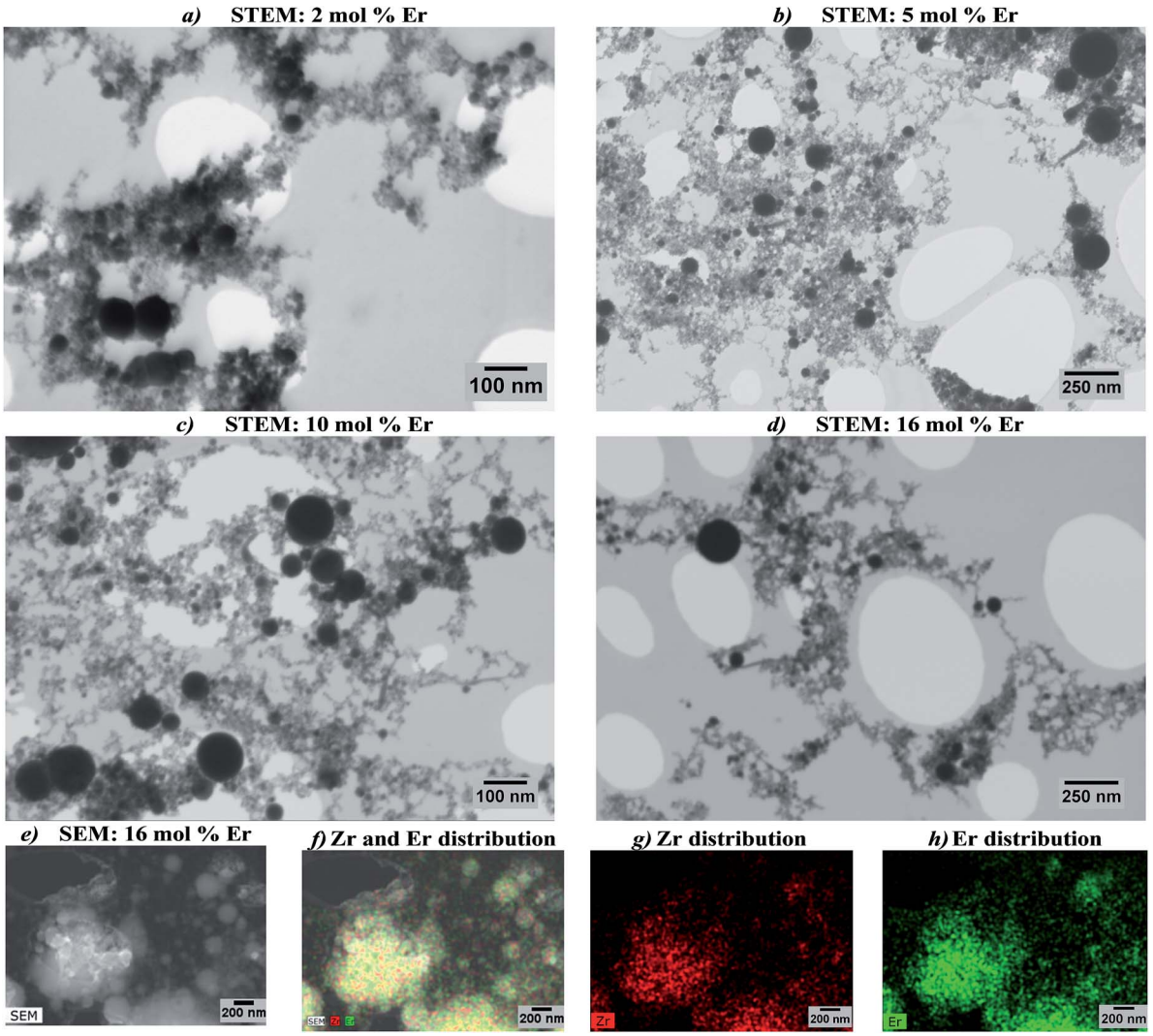

Fig. 3 (a e): STEM/SEM images of the NPs with different dopant concentration. (f h): EDS map of the NPs doped with 16 mol% Er.

distribution. Although the effect of each of these parameters in the NPs size distribution cannot be directly generalized to all materials (since the interaction between the material and the laser beam strongly depends on the materials physical properties), it is expected to be possible to control the average size and size distribution in the doped ZrO_2 NPs as achieved for other oxides NPs produced by PLAL. Concerning the morphology, no differences were observed with the increase of dopant amount. The EDS analysis revealed a uniform distribution of the erbium ions in the produced zirconia nanoparticles (Fig. 3(f–h)) meaning that the high pressure and high temperature environment conditions created by the laser ablation in water is fast enough to preserve the erbium in the zirconia network.

3.2. Optical properties

3.2.1. Photoluminescence excitation. Fig. 4(a) displays the PL and PLE spectra of erbium doped zirconia targets. In all the doped samples, intraionic Er^{3+} emission is observed meaning that independently of the used erbium amount and zirconia crystalline phase, Er^{3+} optically activation is achieved. In order to identify the preferential pathways for the ions luminescence, the PLE spectra were monitored in the blue and green spectral regions. The latter corresponds to the $^4S_{3/2} \rightarrow {}^4I_{15/2}$ transition of the Er^{3+} ions. In the case of the blue luminescence, depending on the ion content (and thus on the zirconia crystalline phase), the PLE was monitored or at the maxima of an intrinsic broad PL band (for lower erbium contents) or on the maxima of the $^2P_{3/2} \rightarrow {}^4I_{11/2}$ Er^{3+} transition (for samples with higher erbium amounts). The PLE data taken from the green $^4S_{3/2} \rightarrow {}^4I_{15/2}$ transition, with maxima at ~561 nm, indicates that the population paths of the Er^{3+} luminescence occur both *via* a broad violet charge transfer (CT) excitation band and under resonant excitation conditions *via* the Er^{3+} excited multiplets. For samples in the monoclinic phase, with lower erbium amounts, the intraionic Er^{3+} luminescence is preferentially populated *via* the CT band peaked between 270–280 nm. Similarly, the broad host-related PL band due to native defects[60 63] is also excited by broad excitation bands with their peak position

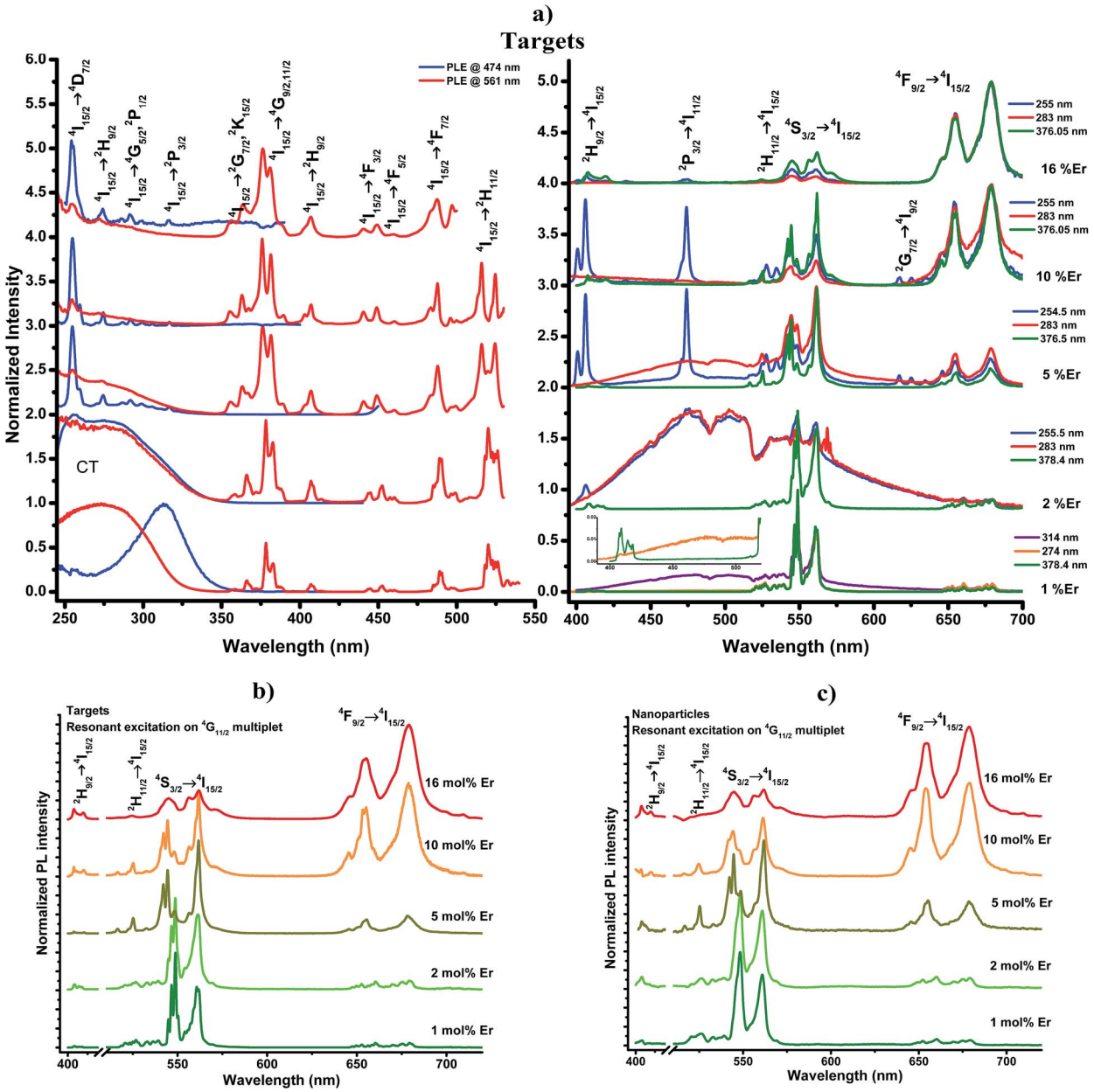

Fig. 4 (a) PLE (left side) and PL (right side) spectra of the erbium doped ZrO_2 targets. The PLE spectra were monitored at the green ($^4S_{3/2} \rightarrow {}^4I_{15/2}$ Er^{3+} transition) and blue (broad band at ~474 nm and $^2P_{3/2} \rightarrow {}^4I_{11/2}$ Er^{3+} transition) spectral regions. The PL was recorded by pumping the samples into the charge transfer excitation band (CT), $^4D_{7/2}$ and $^4G_{11/2}$ Er^{3+} multiplets. (b and c) PL spectra of the targets and PLAL produced NPs obtained with resonant excitation into the $^4G_{11/2}$ level.

dependent on the ion content. For higher erbium concentrations, and in the studied spectral region, a general trend is observed: the decrease of the intensity of the CT excitation band results in changes in the preferential population of the Er^{3+} ion luminescence. For the high lattice symmetry of the tetragonal and cubic zirconia polymorphs, the resonant excitation into the ion excited multiplets dominates the excitation pathways or the Er^{3+} luminescence. The measured PLE spectra also corroborate the aforementioned increase in the bandgap energy of the zirconia host with the crystalline phase transformation from monoclinic to tetragonal and cubic.

3.2.2. Prompt luminescence. The samples luminescence obtained with excitation in the ultraviolet CT band and resonantly into the Er^{3+}, $^4G_{11/2}$ and $^4D_{7/2}$ excited multiplets, is depicted in the right side of Fig. 4(a). The PL response is sensitive either to the excitation energy and erbium content. With excitation into the CT band, the PL spectra of the samples doped with lower erbium content correspond to an overlap of the broad emission band from native defects[60 63] with the sharper intraionic emission lines of Er^{3+}. Additionally, intraionic photon re-absorption is identified. The intensity of the broad band PL decreases with increasing erbium concentration,

as identified for samples doped with higher erbium amounts. Pumping the samples in the highest energetic Er^{3+} multiplet peaked at 255 nm ($^4D_{7/2}$) violet ($^2H_{9/2} \rightarrow {}^4I_{15/2}$), blue ($^2P_{3/2} \rightarrow {}^4I_{11/2}$), green ($^2H_{11/2}$, $^4S_{3/2} \rightarrow {}^4H_{15/2}$) and red light ($^2G_{7/2} \rightarrow {}^4I_{9/2}$; $^4F_{9/2} \rightarrow {}^4I_{15/2}$) are promoted, namely for samples with the tetragonal crystalline structure. For a resonant excitation into the $^4G_{11/2}$ multiplet (~378 nm) the PL spectra are only constituted by three groups of intraionic emission lines: the violet, green and red transitions arising from the $^2H_{9/2}$, $^2H_{11/2}$, $^4S_{3/2}$ and $^4F_{9/2}$ excited states to the $^4I_{15/2}$ ground state, respectively. With the used excitation conditions, the intensity of the Er^{3+} prompt luminescence was found to be dependent on the ion amount and consequently on the crystalline phase. For lower erbium concentrations, where the monoclinic zirconia phase dominates, the radiative recombination in the visible range mainly occurs between the $^4S_{3/2}$ level and the ground state resulting in a green visual appearance in the reference targets and nanoparticles, Fig. 4(b and c). The change in the crystalline phase due to higher erbium concentration is accompanied by a relative increase of the red light due to the $^4F_{9/2} \rightarrow {}^4I_{15/2}$ transition. A likely explanation to the identified behavior is related with the promotion of ion–ion interactions favored for higher dopant concentrations, potentiating energy transfer processes among the interacting defects.[15,64 68] Particularly, nonradiative energy transfer processes, such as resonant phonon assisted transfer and cross relaxation mechanisms among the nearby ions are commonly observed in lanthanide doped wide band gap hosts leading, in some cases, to self-luminescence quenching when the interaction occurs among ions from the same chemical specie.[15,65 68] For instance, the depletion of $^2H_{11/2}$, $^4S_{3/2}$ states to the $^4F_{9/2}$ level by multiphonon de-excitation and cross relaxation processes such those involving the population of the $^4I_{13/2}$ and $^4I_{11/2}$ long lived intermediate levels which in turn repopulates the $^4F_{9/2}$ by energy transfer encompassing ground state absorption (GSA) from a near neighboring ion, justifies the decrease in the intensity of the green light.[15,65 69] The occurrence of such mechanisms pave the way to the development of tunable visible color (green to red) ZrO_2 nanophosphors through the manipulation of the erbium ions concentration, envisaging the use of these nanophosphors in luminescence based biolabels. For such purposes, the control of the luminescence processes with infrared excitation is desirable and efficient RT up-conversion luminescence should be achieved.

3.2.3. Up-conversion mechanisms. Fig. 5(a) shows the green and red emission in the ZrO_2:Er samples after exciting the doped targets and nanoparticles with low energy photons (980 nm), into the $^4I_{11/2}$ multiplet. As for the prompt emission, the up-conversion phenomena allow the identification with a naked eye of the tunable green to red luminescence by increasing the erbium content, Fig. 5. Assuming ground state absorption, the Er^{3+} ions are excited into an intermediate state, the $^4I_{11/2}$ multiplet, which is known to have a long decay time.[70] Therefore, when a second photon is absorbed the $^4I_{11/2}$ level is still populated and considering a model of a sequential absorption of two 980 nm photons involving GSA and excited state absorption (ESA) the $^4I_{15/2} \rightarrow {}^4I_{11/2} \rightarrow {}^4F_{7/2}$ transitions are favored.[15] Moreover, up-conversion processes are also mediated by sequential energy transfer (APTE),[65,66] likewise called as energy transfer up-conversion (ETU).[68] From the $^4F_{7/2}$ multiplet nonradiative multiphonon relaxation to the $^4S_{3/2}$ and $^4F_{9/2}$ excited states occur with further green and red radiative de-excitation to the ground state. A second route to the population of the $^4F_{9/2}$ excited state can be considered after the $^4I_{15/2} \rightarrow {}^4I_{11/2}$ absorption, namely *via* sequential nonradiative relaxation from the $^4I_{11/2}$ to the $^4I_{13/2}$ multiplet, followed by excited state absorption and sequential energy transfer to the higher energetic multiplet from where the red emission originates (Fig. 5(b)).

To investigate the up conversion luminescence mechanisms, the excitation power dependence of the green and red up-converted PL spectra were carried out. The excitation power dependence of the integrated green and red light of the reference targets and PLAL doped nanoparticles are shown in the log–log plots in Fig. 6(a). It is well established[15,65 69,71] that the up-converted emission intensity scales with a power law, $I \propto P^n$, where P corresponds to the excitation power and n is the number of photons involved on the process, which in the analyzed ZrO_2:Er samples ranges between $1 > n > 2$, agreeing well with the rate equations model of Pollnau *et al.*[71] Here, the intensity of the emitting state follows a P^n law for systems where the up-conversion (APTE (ETU)/ESA) mechanisms could be neglected in the intermediate states and adopt a P^1 law in systems where the same up-conversion processes dominates.[15,66,67,69,71] As such, a unitary slope of the luminescence intensity is expected to occur with increasing power excitation. Besides these two limit situations, real cases can be located in an intermediate regime, where a competition between the radiative and nonradiative depletion of an intermediate state arises, leading to slopes among the two mentioned values.[15,66,67,69,71] The described processes clearly influence the excitation to or the depletion from a given emitting level, yielding to distinct observed phenomena in the description of the up converted light. Besides the aforementioned mechanisms, additional processes (*e.g.* cross relaxation mechanisms) also influence the intensity of the up converted luminescence, as earlier reported by Auzel[65,66,69] and Pollnau *et al.*[71] The data shown in Fig. 6 allows further investigation about the dominating processes involved in the up-conversion process for the ZrO_2:Er samples. As a starting point, it should be emphasized that either for the green or red luminescence none of the measured slopes corresponds to $n = 2$. This corresponds to the case where a linear decay from the intermediate levels is expected and the up-conversion processes are insignificant. However, the higher slope tendency observed for the green $^4S_{3/2} \rightarrow {}^4I_{15/2}$ multiplet transition in samples with lower erbium concentration, suggests that the radiative decay is the dominant process involved on the energetic depopulation of intermediate levels, instead of the competitive up-conversion processes. As such, the values close to $n = 2$ reflect the photon excitation steps for the population of the $^4S_{3/2}$ level. On the other hand, the measured slope for the red luminescence originated in the $^4F_{9/2}$ multiplet for the same set of samples (lower amount of erbium ions) is slightly lower than those of the green emission. As above mentioned the tendency for a lower intermediate n value, means that a higher competition

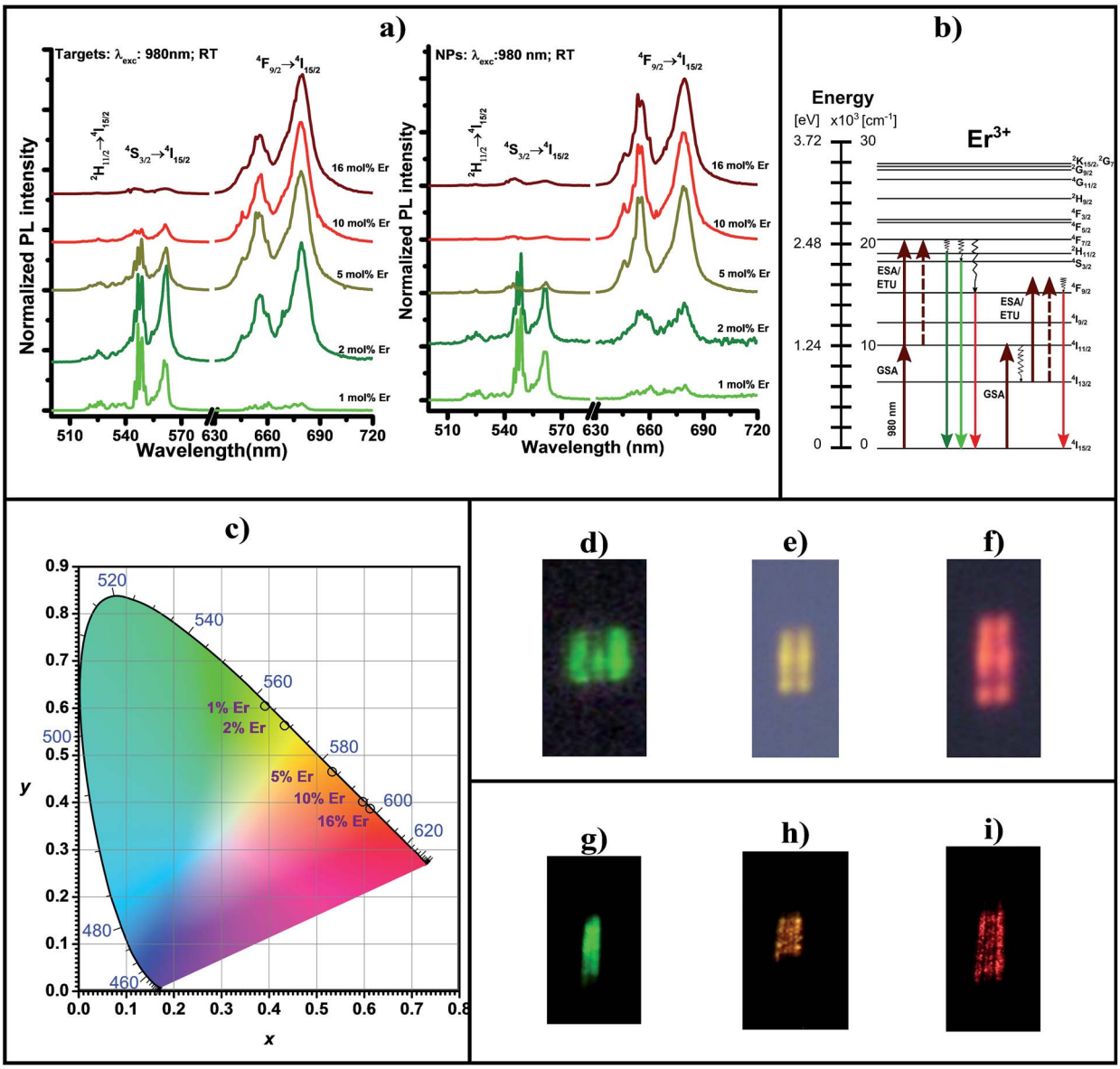

Fig. 5 (a) PL spectra of the targets (left) and the PLAL produced NPs (right) obtained with 980 nm wavelength excitation photons. (b) Schematic energy level diagram for Er^{3+} ions illustrating the up-converted luminescence. (c) Color diagram coordinates with the representation of the overall up-conversion emission for the different erbium amounts. Photographs of the RT up converted luminescence of (d) 1 mol% (e) 2 mol% and (f) 16 mol% targets and (g) 1 mol% (h) 5 mol% and (i) 16 mol% nanoparticles, after dried on top of a quartz subtract, with 980 nm excitation.

occurs among the radiative depletion of the intermediate states and the up-conversion processes. For instance, besides the $^4I_{15/2} \rightarrow {}^4I_{11/2} \rightarrow {}^4F_{7/2}$ path (involved on the population of the $^4S_{3/2}$ and $^4F_{9/2}$ multiplets) a likely mechanism for the population of the $^4F_{9/2}$ state corresponds to the two step excitation following the $^4I_{15/2} \rightarrow {}^4I_{11/2} \rightarrow {}^4I_{13/2} \rightarrow {}^4F_{9/2}$ route, with nonradiative relaxation among the $^4I_{11/2}$ and $^4I_{13/2}$ states. As both processes own for different probability rates a different slope for the red emission intensity is expected when compared with the green one, suggesting a higher competition among the up-conversion mechanisms and the radiative decay of the intermediate level to the ground state.

Fig. 6(b) shows the concentration dependence of the slope of the green and red up converted light whereas the red/green luminescence intensity ratio for the prompt and up-conversion Er^{3+} luminescence is shown in Fig. 6(c). A linear decrease slope tendency of the green and the red up-converted light emission is observed and the composition dependence of the red/green intensity ratio follows a linear behavior for low erbium contents and a supralinear trend for higher amounts. The slope tendency, with a value close to the unity for the highest doped samples, favors the assumption that large up-conversion rates arise for the highest doped samples reflecting the role of the increase in the lattice symmetry (from

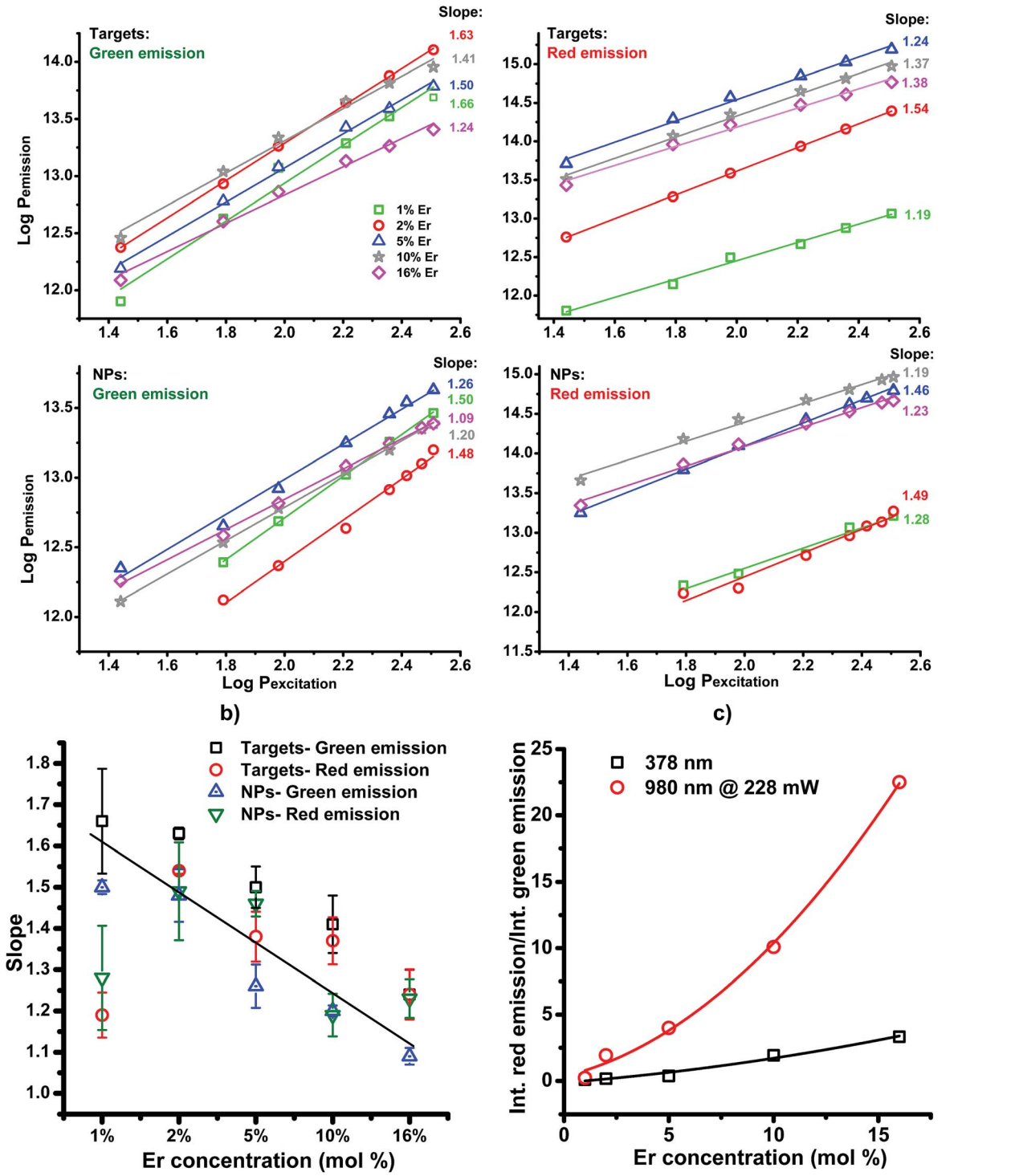

Fig. 6 (a) Excitation power dependence of the integrated green and red RT up-converted luminescence for the erbium doped zirconia samples with different erbium amounts. The excitation was performed with 980 nm wavelength photons corresponding to the GSA $^4I_{15/2} \rightarrow {}^4I_{11/2}$. (b) Er concentration dependence of the slope of the green and red up-converted light. (c) red/green intensity ratio for the prompt (378 nm excitation) and up-conversion Er^{3+} emission (980 nm excitation at 228 mW).

monoclinic → monoclinic + tetragonal → tetragonal → cubic) and ion site location on the transition probability rates of the observed emission. On the other hand, and for samples with higher erbium amounts, a promotion of the red $^4F_{9/2} \rightarrow {}^4I_{15/2}$ transition was found, either in prompt and up-conversion luminescence. As aforementioned for the prompt luminescence this behavior leads us to consider that the suppression of the green emission could involve additional nonradiative pathways for the depopulation of the $^4S_{3/2}$. On the other hand, considering the excitation with low energy 980 nm photons the increase in the

population of the $^4I_{11/2,\ 13/2}$ results in enhanced red emission intensity as observed in other sesquioxides such as Y_2O_3.[72]

4. Conclusions

In conclusion, we have reported the tunable visible color (green to red) ZrO_2:Er nanophosphors through the manipulation of the erbium ions concentration. The synthesis of the doped nanoparticles was successfully achieved by pulsed laser ablation in water using ZrO_2:Er sintered targets constituting a reliable and controllable way for the optically activation of dopants in nanosized zirconia. Analytical investigation by Raman spectroscopy, photoluminescence, photoluminescence excitation and scanning transmission electron microscopy has shown the structural, morphological and optical quality of the produced nanoparticles. As expected, different polymorphs (monoclinic to cubic crystalline phases) of ZrO_2:Er were promoted increasing the amount of dopant as identified by the Raman spectroscopy. No other crystalline oxides were found even for high nominal erbium contents proving that a uniform incorporation of the Er^{3+} ions in the ZrO_2 lattice was achieved as observed by EDS. ZrO_2:Er nanoparticles present spherical shape and particle sizes up to 200 nm. No differences in nanoparticles morphology were observed with the change in the crystalline structure of the zirconia as a result of erbium addition. Detailed studies of the prompt and up conversion Er^{3+} luminescence showed that using high and low energy photons as excitation, the dominant visible luminescence of the Er^{3+} ions in zirconia nanoparticles occurs in the green and red regions due to transitions from the $^4S_{3/2}$ and $^4F_{9/2}$ multiplets to the $^4I_{15/2}$ ground state, respectively. The number of the green emission Stark levels was found to decrease with increasing erbium amount as expected for ions placed in high symmetry sites following the crystalline host phase transformation. Additionally, the green to red luminescence intensity ratio was found to be dependent of the erbium amount, accompanying the increase in the lattice symmetry. The suppression of the green transition for higher concentrations was discussed based on nonradiative competitive mechanisms such as cross relaxation processes between near neighboring ions as expected for higher dopant contents. The power dependence of the visible Er^{3+} up-conversion emission reveals slopes between 1 and 2 meaning that competition occurs among the radiative depletion of the intermediate states and the up-conversion mechanisms. The lowest doped samples, showing a dominant green light, evidence higher slope suggesting small up-conversion rates. On the opposite side, the highest doped samples (those where the red emission prevails) exhibit a slope near the unity. In both cases, the visual appearance of the green and red up-converted light is clearly observed at room temperature with naked eye. This investigation is helpful to understand the mechanisms behind the prompt and up conversion luminescence of ZrO_2:Er^{3+} nanoparticles and a way to further improve the material design for tunable green to red zirconia based nanophosphors was found.

Acknowledgements

The authors acknowledge FCT for the final funding from PEst-C/CTM/LA0025/2013–14, CENTRO-07-ST24-FEDER-002030, PTDC/CTM-NAN/2156/2012 and RECI/FIS-NAN/0183/2012 (FCOMP-01-0124-FEDER-027494) projects. M. R. N. Soares thank FCT for her PhD grant, SFRH/BD/80357/2011.

Notes and references

1 F. Wang, D. Banerjee, Y. Liu, X. Chen and X. Liu, *Analyst*, 2010, **135**, 1839–1854.
2 S. V. Eliseeva and J.-C. G. Bünzli, *Chem. Soc. Rev.*, 2010, **39**, 189–227.
3 P. Hänninen and H. Härmä, *Lanthanide Luminescence: Photophysical, Analytical and Biological Aspects*, Springer Science & Business Media, 2011.
4 D. Tu, W. Zheng, Y. Liu, H. Zhu and X. Chen, *Coord. Chem. Rev.*, 2014, **273–274**, 13–29.
5 M. V. DaCosta, S. Doughan, Y. Han and U. J. Krull, *Anal. Chim. Acta*, 2014, **832**, 1–33.
6 W. Zheng, P. Huang, D. Tu, E. Ma, H. Zhu and X. Chen, *Chem. Soc. Rev.*, 2014, DOI: 10.1039/c4cs00178h.
7 F. Zhang, *Photon Upconversion Nanomaterials*, Springer, 2015.
8 C. T. Xu, Q. Zhan, H. Liu, G. Somesfalean, J. Qian, S. He and S. Andersson-Engels, *Laser Photonics Rev.*, 2013, **7**, 663–697.
9 J. Chen and J. X. Zhao, *Sensors*, 2012, **12**, 2414–2435.
10 F. Gonell, M. Haro, R. S. Sánchez, P. Negro, I. Mora-Seró, J. Bisquert, B. Julián-López and S. Gimenez, *J. Phys. Chem. C*, 2014, **118**, 11279–11284.
11 F. Wang and X. Liu, in *Comprehensive Nanoscience and Technology*, ed. D. L. Andrews, G. D. Scholes and G. P. Wiederrecht, Academic Press, Amsterdam, 2011, pp. 607–635.
12 V. K. A. Sreenivasan, A. V. Zvyagin and E. M. Goldys, *J. Phys.: Condens. Matter*, 2013, **25**, 194101.
13 M. Lin, Y. Zhao, S. Wang, M. Liu, Z. Duan, Y. Chen, F. Li, F. Xu and T. Lu, *Biotechnol. Adv.*, 2012, **30**, 1551–1561.
14 S. Hao, G. Chen and C. Yang, *Theranostics*, 2013, **3**, 331–345.
15 J. F. Suijver, in *Luminescence*, ed. C. Ronda, Wiley-VCH Verlag GmbH & Co. KGaA, 2007, pp. 133–177.
16 M. Haase and H. Schäfer, *Angew. Chem., Int. Ed.*, 2011, **50**, 5808–5829.
17 F. Vetrone and J. A. Capobianco, *Int. J. Nanotechnol.*, 2008, **5**, 1306–1339.
18 J. A. Capobianco, F. Vetrone, J. C. Boyer, A. Speghini and M. Bettinelli, *J. Phys. Chem. B*, 2002, **106**, 1181–1187.
19 F. Vetrone, J.-C. Boyer, J. A. Capobianco, A. Speghini and M. Bettinelli, *J. Appl. Phys.*, 2004, **96**, 661–667.
20 J. A. Capobianco, F. Vetrone, T. D'Alesio, G. Tessari, A. Speghini and M. Bettinelli, *Phys. Chem. Chem. Phys.*, 2000, **2**, 3203–3207.
21 M. Liu, S. W. Wang, J. Zhang, L. Q. An and L. D. Chen, *Opt. Mater.*, 2007, **29**, 1352–1357.
22 F. Vetrone, J. C. Boyer, J. A. Capobianco, A. Speghini and M. Bettinelli, *J. Phys. Chem. B*, 2002, **106**, 5622–5628.

23 V. Venkatramu, D. Falcomer, A. Speghini, M. Bettinelli and C. K. Jayasankar, *J. Lumin.*, 2008, **128**, 811–813.
24 V. Mahalingam, F. Mangiarini, F. Vetrone, V. Venkatramu, M. Bettinelli, A. Speghini and J. A. Capobianco, *J. Phys. Chem. C*, 2008, **112**, 17745–17749.
25 A. Patra, S. Saha, M. A. R. C. Alencar, N. Rakov and G. S. Maciel, *Chem. Phys. Lett.*, 2005, **407**, 477–481.
26 A. Patra, C. S. Friend, R. Kapoor and P. N. Prasad, *J. Phys. Chem. B*, 2002, **106**, 1909–1912.
27 L. A. Gómez, L. D. S. Menezes, C. B. de Araújo, R. R. Gonçalves, S. J. L. Ribeiro and Y. Messaddeq, *J. Appl. Phys.*, 2010, **107**, 113508.
28 D. Solis, E. D. la Rosa, O. Meza, L. A. Diaz-Torres, P. Salas and C. Angeles-Chavez, *J. Appl. Phys.*, 2010, **108**, 023103.
29 F. Gallino, C. Di Valentin and G. Pacchioni, *Phys. Chem. Chem. Phys.*, 2011, **13**, 17667.
30 M. R. N. Soares, C. Nico, M. Peres, N. Ferreira, A. J. S. Fernandes, T. Monteiro and F. M. Costa, *J. Appl. Phys.*, 2011, **109**, 013516.
31 E. De la Rosa, L. A. Diaz-Torres, P. Salas and R. A. Rodríguez, *Opt. Mater.*, 2005, **27**, 1320–1325.
32 Y. Liu, S. Zhou, D. Tu, Z. Chen, M. Huang, H. Zhu, E. Ma and X. Chen, *J. Am. Chem. Soc.*, 2012, **134**, 15083–15090.
33 J. Shen, L.-D. Sun and C.-H. Yan, *Dalton Trans.*, 2008, 5687–5697.
34 G. Yang, *Laser Ablation in Liquids: Principles and Applications in the Preparation of Nanomaterials*, CRC Press, 2012.
35 P. V. Kazakevich, A. V. Simakin, V. V. Voronov and G. A. Shafeev, *Appl. Surf. Sci.*, 2006, **252**, 4373–4380.
36 T. E. Itina, *J. Phys. Chem. C*, 2011, **115**, 5044–5048.
37 H. Zeng, X.-W. Du, S. C. Singh, S. A. Kulinich, S. Yang, J. He and W. Cai, *Adv. Funct. Mater.*, 2012, **22**, 1333–1353.
38 T. Tsuji, M. Nakanishi, T. Mizuki, M. Tsuji, T. Doi, T. Yahiro and J. Yamaki, *Appl. Surf. Sci.*, 2009, **255**, 9626–9629.
39 T. Maldiney, G. Sraiki, B. Viana, D. Gourier, C. Richard, D. Scherman, M. Bessodes, K. Van den Eeckhout, D. Poelman and P. F. Smet, *Opt. Mater. Express*, 2012, **2**, 261–268.
40 T. Nunokawa, Y. Onodera, M. Hara, Y. Kitamoto, O. Odawara and H. Wada, *Appl. Surf. Sci.*, 2012, **261**, 118–122.
41 G. Ledoux, D. Amans, C. Dujardin and K. Masenelli-Varlot, *Nanotechnology*, 2009, **20**, 445605.
42 S. A. Al-Mamun and T. Ishigaki, *J. Am. Ceram. Soc.*, 2014, 1–8.
43 Y. Onodera, T. Nunokawa, O. Odawara and H. Wada, *J. Lumin.*, 2013, **137**, 220–224.
44 S. K. Singh, K. Kumar and S. B. Rai, *Mater. Sci. Eng., B*, 2010, **166**, 180–184.
45 F. Yoshimura, K. Nakamura, F. Wakai, M. Hara, M. Yoshimoto, O. Odawara and H. Wada, *Appl. Surf. Sci.*, 2011, **257**, 2170–2175.
46 X. C. Yang, W. Riehemann, M. Dubiel and H. Hofmeister, *Mater. Sci. Eng., B*, 2002, **95**, 299–307.
47 D. Tan, G. Lin, Y. Liu, Y. Teng, Y. Zhuang, B. Zhu, Q. Zhao and J. Qiu, *J. Nanopart. Res.*, 2011, **13**, 1183–1190.
48 N. Bärsch, J. Jakobi, S. Weiler and S. Barcikowski, *Nanotechnology*, 2009, **20**, 445603.
49 D. Tan, Y. Teng, Y. Liu, Y. Zhuang and J. Qiu, *Chem. Lett.*, 2009, **38**, 1102–1103.
50 M. R. N. Soares, C. Nico, D. Oliveira, M. Peres, L. Rino, A. J. S. Fernandes, T. Monteiro and F. M. Costa, *Mater. Sci. Eng., B*, 2012, **177**, 712–716.
51 E. Fernández López, V. Sánchez Escribano, M. Panizza, M. M. Carnasciali and G. Busca, *J. Mater. Chem.*, 2001, **11**, 1891–1897.
52 E. Djurado, P. Bouvier and G. Lucazeau, *J. Solid State Chem.*, 2000, **149**, 399–407.
53 S. Shukla, S. Seal, R. Vij, S. Bandyopadhyay and Z. Rahman, *Nano Lett.*, 2002, **2**, 989–993.
54 S. Shukla and S. Seal, *Rev. Adv. Mater. Sci.*, 2003, **4**, 123–126.
55 C. Liu, X. L. Mao, S. S. Mao, X. Zeng, R. Greif and R. E. Russo, *Anal. Chem.*, 2004, **76**, 379–383.
56 S. Alves, M. Kalberer and R. Zenobi, *Rapid Commun. Mass Spectrom.*, 2003, **17**, 2034–2038.
57 V. Amendola and M. Meneghetti, *Phys. Chem. Chem. Phys.*, 2013, **15**, 3027–3046.
58 S. A. Al-Mamun, R. Nakajima and T. Ishigaki, *J. Colloid Interface Sci.*, 2013, **392**, 172–182.
59 S. A. Al-Mamun, R. Nakajima and T. Ishigaki, *Thin Solid Films*, 2012, **523**, 46–51.
60 S. E. Paje and J. Llopis, *Appl. Phys. A*, 1993, **57**, 225–228.
61 N. G. Petrik, D. P. Taylor and T. M. Orlando, *J. Appl. Phys.*, 1999, **85**, 6770–6776.
62 H. Nakajima and T. Mori, *J. Alloys Compd.*, 2006, **408–412**, 728–731.
63 E. De la Rosa-Cruz, L. Díaz-Torres, P. Salas, D. Mendoza, J. Hernández and V. Castaño, *Opt. Mater.*, 2002, **19**, 195–199.
64 B. G. Wybourne, *Spectroscopic Properties of Rare Earths*, Interscience Publishers, New York, 1965, vol. 148.
65 F. E. Auzel, *Proc. IEEE*, 1973, **61**, 758–786.
66 F. Auzel, *Chem. Rev.*, 2004, **104**, 139–174.
67 G. Liu and B. Jacquier, *Spectroscopic Properties of Rare Earths in Optical Materials*, Springer, 2006.
68 J. C. Wright, in *Radiationless Processes in Molecules and Condensed Phases*, Springer, Berlin Heidelberg, 1976, pp. 239–295.
69 F. Auzel, P. A. Santa-Cruz and G. F. de Sá, *Rev. Phys. Appl.*, 1985, **20**, 273–281.
70 F. Vetrone, J.-C. Boyer, J. A. Capobianco, A. Speghini and M. Bettinelli, *Appl. Phys. Lett.*, 2002, **80**, 1752–1754.
71 M. Pollnau, D. R. Gamelin, S. R. Lüthi, H. U. Güdel and M. P. Hehlen, *Phys. Rev. B: Condens. Matter Mater. Phys.*, 2000, **61**, 3337–3346.
72 H. Lu, W. P. Gillin and I. Hernández, *Phys. Chem. Chem. Phys.*, 2014, **16**, 20957–20963.